Surface & Coatings Technology 516 (2025) 132668

Contents lists available at ScienceDirect

Surface & Coatings Technology

journal homepage: www.elsevier.com/locate/surfcoat

Full Length Article

Influence of Si content on cracking behavior of CrAlSiN coatings☆

Kirsten Bobzin, Max Philip Möbius, Jessica Borowy *

Surface Engineering Institute, RWTH Aachen University, Kackertstr. 15, 52072, Aachen, Germany

ARTICLE INFO

Keywords:
PVD
Nanoindentation
Cracking behavior
CrAlSiN
Cutting tool
Milling

ABSTRACT

Physical Vapor Deposition (PVD) manufactured CrAlSiN nanocomposite coatings, composed of CrAlN grains in a SiN_x matrix, represent a promising solution for improved cutting performance of milling tools. The elastic-plastic properties and deformation behavior of the material composite thereby can be deliberately influenced by varying the silicon content.

CrAlSiN coatings with silicon contents of $x_{Si} = 10$, 16, 22, and 29 at.-% in the metal portion were fabricated on cemented carbide WC-Co substrates. The indentation hardness H_{IT} and modulus E_{IT} of the coatings were measured through nanoindentation, using a Berkovich indenter. Additionally, crack resistance was evaluated using high load (HL) nanoindentation tests under forces ranging from $F_{HL} = 750$ to 1750 mN, using a conical diamond indenter. The findings reveal that the indentation hardness H_{IT} remains unchanged at $H_{IT} = (25.5 \pm 1.6)$ GPa, while the indentation modulus increases with higher silicon content. After high load nanoindentation all coatings exhibit no cracks at $F_{HL} = 750$ mN. Initial cracks are observed at $F_{HL} = 1000$ mN for $x_{Si} = 10$ at.-%, whereas they appear at just $F_{HL} = 800$ mN for $x_{Si} = 29$ at.-%. With a further increase in load to $F_{HL} = 1750$ mN, it is evident that the coating with a silicon content of $x_{Si} = 22$ at.-% displays the fewest and shortest cracks.

Coatings with high silicon content therefore demonstrate promising crack resistance at room temperature even though the examination of indentation hardness and modulus does not support this behavior at first sight. This highlights their potential for further investigation, qualifying these coatings for additional studies under high-temperature conditions, aiming to enhance their applicability in machining processes.

1. Introduction

The constantly increasing demands for workpiece quality and economic efficiency in machining processes necessitate a comprehensive consideration of all relevant influencing variables. In addition to cutting parameters, the materials being machined, the materials of cutting tools, tool geometry, and tool coatings play a crucial role. These coatings are applied to tools to counteract the complex load spectrum encountered during machining by enhancing wear resistance and thermal stability.

The primary damage mechanisms during machining include adhesion, abrasion, tribochemical reactions, diffusion, and surface disintegration. Tool coatings significantly increase the resistance of tools to these detrimental effects, enabling industries to employ more demanding cutting parameters such as higher cutting speeds. This capability ultimately leads to increased productivity and cost-effectiveness in manufacturing processes.

Based on binary hard coatings such as CrN or TiN, aluminum and silicon have been utilized to develop quaternary systems such as CrAlSiN. CrAlSiN coatings produced via physical vapor deposition (PVD) exhibit promising properties that address the challenges faced in machining applications. According to Endrino et al., silicon tends to replace chromium in the face-centered cubic (fcc) Cr–Al–N lattice at low silicon contents of $x_{Si} = 5$ at.-% within CrAlSiN coatings [1]. This conclusion is drawn by their X-ray absorption spectroscopy (XAS) measurements, which reveal transitions from Cr-1 s states to Cr-3d states hybridized with Si-2p empty states. These observations indicate that the incorporation of silicon results in significant changes in the electronic structure and local environment of the atoms, facilitating the substitution of chromium within the lattice. The similar atomic radii of chromium and silicon may facilitate this substitution. However, it should be noted that silicon adopts an A4-type structure with typically four valence electrons, whereas chromium exhibits a B1-type structure with usually two, three, or six valence electrons. This factor raises doubts about the feasibility of silicon effectively replacing chromium atoms in

☆ This article is part of a Special issue entitled: 'ICMCTF 2025 (SCT)' published in Surface & Coatings Technology.

* Corresponding author.
E-mail address: borowy@iot.rwth-aachen.de (J. Borowy).

https://doi.org/10.1016/j.surfcoat.2025.132668
Received 10 June 2025; Received in revised form 8 September 2025; Accepted 10 September 2025
Available online 11 September 2025

the lattice. Additionally, Bashilia et al. demonstrated using X-ray photoelectron spectroscopy (XPS) that at a silicon content of $x_{Si} = 7.5$ at.-% silicon exists solely in an amorphous Si_3N_4 bonding environment, resulting in a nanocomposite structure composed of CrAlN grains surrounded by this amorphous phase [2]. In the authors' view, this observation makes it more likely that silicon does not participate in forming a crystalline structure within the coating. The amorphous Si_3N_4 phase thereby inhibits the growth of the CrAlN grains to d < 20 nm [3].

Oxidation is one key factor influencing the performance of coatings on tools used in machining applications. The oxidation resistance of CrAlSiN, TiAlSiN and Cr-Mo-V tool steel was investigated in different studies by Chaliampalias et al. The CrAlSiN coatings exhibited significant oxidation resistance, with oxidation starting at temperatures above $T_O = 900$ °C [4]. In contrast, the Cr–Mo–V tool steel showed signs of oxidation beginning at lower temperatures, around $T_O = 600$ °C [5]. For the TiAlSiN coatings, oxidation initiated at approximately $T_O = 700$ °C [6]. These findings highlight that CrAlSiN coatings provide superior protection against oxidation at elevated temperatures compared to both traditional tool steel and TiAlSiN coatings. This is due to the fact that the Si_3N_4 phase in the coatings has a better resistance to oxidation than CrAlN coatings. Oxidation of amorphous Si_3N_4 starts at $T = 1300$ °C [7] whereas the onset of oxidation of CrAlN coatings is observable at $T = 900$ °C [8]. A CrAlSiN coating with $x_{Si} = 16$ at.-% demonstrates the highest onset temperature for oxidation while exhibiting the lowest weight gain when compared to CrAlSiN coatings with lower silicon content as well as CrAlN coatings [9]. For the same coatings indentation hardness at room temperature increases with rising silicon content up to $x_{Si} = 8$ at.-%, with only a slight reduction at $x_{Si} = 16$ at.-%. At the same time, the reduction in hardness of CrAlSiN coatings with a silicon content of $x_{Si} = 9.3$ at.-% is lower at high in situ temperatures $T \geq 500$ °C compared to CrAlN [10], which indicates improved thermal stability. In addition, CrAlSiN coatings can improve the resistance of the composite to tribooxidation [11]. While the wear for both CrAlN and CrAlSiN coatings increases with increasing temperature, the wear coefficients in pin-on-disc (PoD) tests with CrAlSiN coatings and aluminum counter body are on average lower at high temperatures $T \geq 300$ °C compared to CrAlN [10]. This can be attributed to the lower friction in the tribological system, the high resistance to plastic deformation and the high wear resistance of a Si-modified coating with an amorphous structure [12]. Tools with CrAlSiN coating also showed the longest tool life in milling tests of Ti6Al4V compared to TiAlN and TiAlSiN [13].

These findings highlight the significant potential of CrAlSiN coatings for machining applications. However, there are only limited studies on high silicon content $x_{Si} > 10$ at.-% variants of these coatings. To date, according to the authors' knowledge, no investigations have been conducted on the crack resistance of CrAlSiN coatings with varying silicon content. However, the investigation of crack resistance in coatings is crucial for machining applications, as it directly impacts the durability and performance of cutting tools under various operational stresses.

In this study, CrAlSiN coatings with silicon contents of $x_{Si} = 10$, 16, 22, and 29 at.-% in the metal portion were deposited using hybrid high power pulsed magnetron sputtering (HPPMS) and direct current magnetron sputtering (dcMS)technology. HPPMS offers distinct advantages over conventional sputtering technologies such as dcMS due to its plasma characteristics. The higher degree of ionization in HPPMS leads to a greater population of energetic ions, which can significantly influence the coating structure by promoting a denser and more refined microstructure. Additionally, the increased ion energy during deposition enhances the mobility of adatoms on the substrate surface, improving interfacial adhesion and enabling better control over stress states within the coating. The coatings were investigated regarding their indentation hardness H_{IT}, indentation modulus E_{IT}, and crack resistance through nanoindentation techniques. Measurements were performed at room temperature using a Berkovich indenter and a normal load $F_{NI} = 10$ mN for indentation hardness and modulus determination. Additionally, high-load nanoindentation tests using a conical indenter were conducted. To determine the crack resistance, the normal load F_{HL} was varied between 750 mN $\leq F_{HL} \leq$ 1750 mN.

2. Experimental

2.1. Coating deposition

For the deposition of the CrAlSiN coatings, an industrial coating system CC800/9 HPPMS from CemeCon AG, Würselen, Germany, was utilized. The coatings under investigation were deposited using two high power pulsed magnetron sputtering (HPPMS) and two direct current magnetron sputtering (dcMS) cathodes, as shown in Fig. 1. The cathodes were utilized in a close field arrangement along with cathode covers connected to a grounded chamber, as well as electrically insulated cathodes and table arrangements. One CrAl20 target and one Al70Cr30 target were installed on the HPPMS cathodes. The CrAl20 target consists of a chromium base with 20 aluminum plugs. The Al70Cr30 target was produced through powder metallurgy with a composition of $x_{Al} = 70$ at.-% and $x_{Cr} = 30$ at.-%. One silicon target was installed on each dcMS cathode. All processes were conducted consecutively, which means that the formation of the sputtering groove is estimated to be consistent across these runs. As process gas, argon was used, while nitrogen served as reactive gas. The working point is set at the onset of the transition mode between metallic mode and reactive mode. The substrate table rotated at a speed of $n_{Table} = 1$ min^{-1}. Additionally, WC-Co cemented carbide samples were rotated in a three-fold rotation via a satellite on the table and a carrier moved by a kicker. To measure the temperature within the coating chamber, a K-Type thermocouple was employed. The approximate position of the thermocouple inside the coating chamber is indicated in Fig. 1.

Prior to the deposition process WC-Co cemented carbide samples were polished to a surface roughness of 0.02 µm $\leq Sa \leq$ 0.03 µm and subsequently cleaned in ultrasonic cleaning baths. The samples were further cleaned by Ar booster etching as well as middle frequency etching in the coating unit. The process parameters for all CrAlSiN variants are presented in Table 1. The coating architecture consists of a CrAl/CrAlN interlayer, followed by the CrAlSiN functional layer. The silicon content of the investigated coatings was varied by adjusting the power of the dcMS1 and dcMS2 cathode, while the remaining process parameters remained constant.

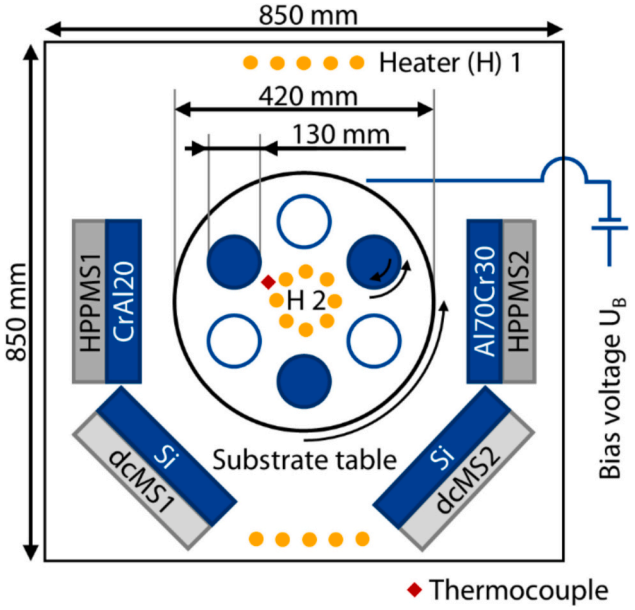

Fig. 1. Schematic of the CC800/9 HPPMS chamber with target configuration.

Table 1
Process parameters of the CrAlSiN coatings with varied silicon content.

Process	ID5189	ID5190	ID5191	ID5192
Pressure p / mPa	530			
Argon flow j_{Ar} / sccm	200			
Nitrogen flow j_{N2} / sccm	Pressure controlled			
Heater power 1 P_{H1} / kW	8.8			
Heater power 2 P_{H2} / kW	4.0			
DC bias voltage U_B / V	−100			
Bias current I_B / A	1.4	1.5	1.6	1.7
Cathode power P_{HPPMS1} / kW	2.2			
Cathode power P_{HPPMS2} / kW	5			
HPPMS Pulse frequency f / Hz	1.000			
HPPMS Pulse duration t_{on} / µs	40			
Cathode power P_{dcMS1} & P_{dcMS2} / kW	**0.55**	**0.85**	**1.15**	**1.45**
Deposition time t / min	**216**	**208**	**208**	**200**
Max. deposition temperature T_{max} / °C	**611**	**612**	**609**	**609**

2.2. Coating and compound characterization

To investigate the coating and compound properties, CrAlSiN coatings were produced on WC-Co cemented carbide substrates. Cross-sections, which were captured using a Zeiss DSM 982 Gemini scanning electron microscope (SEM), Jena, Germany, were used to examine the coating morphology and thickness. The chemical composition of the coatings was measured via electron probe microanalysis (EPMA) with a JEOL JXA-8530, Jeol, Tokyo, Japan, using a linescan over the edge of a calotte to determine the composition throughout the coating thickness. In addition, the microstructure of the coatings was examined using a combination of focused ion beam (FIB) and scanning transmission electron microscopy (STEM). FIB lamellae were prepared by cross-sectioning using PFIB Helios 5, Thermo Fischer Scientific, Eindhoven, Netherlands. Using FEI Tecnai G^2 F20 S-TWIN, Thermo Fischer Scientific, Eindhoven, Netherlands, the FIB lamellae were analyzed by STEM and selected area electron diffraction (SAED) patterns were recorded. The SEM and EPMA investigations as well as FIB preparations and TEM investigations were conducted at the Central Facility for Electron Microscopy (GFE) at RWTH Aachen University, Aachen, Germany. The area average roughness *Sa* as well as the root mean square height *Sq* were measured according to ISO 25178-2:2023 using a confocal laser scanning microscope (CLSM), VKX 210, Keyence Corporation, Osaka, Japan. The adhesion between coating and substrate under static load was characterized by Rockwell A indentation hardness testing according to DIN 4856 using an HP100 Rockwell testing device from KNUTH Machine Tools GmbH, Wasbek, Germany. The tests were conducted with a diamond indenter featuring a cone angle of $\Theta = 120°$ and a normal force of F = 588.4 N. The indents were analyzed using CLSM to determine the adhesion strength class (HF). The interfacial adhesion of the coatings under dynamic load was investigated through constant-force scratch tests according to DIN EN ISO 20502:2016. Tests were performed with a sliding speed of $v_s = 10$ mm/min and normal forces increasing from $F = 10$ N to $F = 100$ N in increments of $\Delta F = 10$ N. A diamond indenter mounted on a scratch tester HPG 200/2 from Gesellschaft für Fertigungstechnik und Entwicklung Schmalkalden e.V., Schmalkalden, Germany was used for this purpose. Scratch tracks were analyzed for cracks and delamination using CLSM.

2.3. Nanoindentation

The indentation hardness H_{IT} and indentation modulus E_{IT} of the coatings were measured by nanoindentation according to ISO 14577-1:2015. A Berkovich diamond indenter with a nominal radius of $r = 150$ nm mounted on a Triboindenter TI 950 from Bruker Corporation, Billerica, Massachusetts, USA was used for this purpose. For each variant, 50 measurements with a maximum indentation force of $F_{max} = 10$ mN were performed. The resulting force-displacement data were used to calculate the mean H_{IT} and E_{IT} values using the method of Oliver and Pharr [14]. A Poisson's ratio of $\nu = 0.25$ was assumed for the calculations [15].

To investigate the deformation behavior of the coatings under quasi-static loading, indents were made using high load nanoindentation at maximum indentation force F_{HL} varied between 750 mN $\leq F_{HL} \leq$ 1000 mN with $\Delta F_{HL} = 50$ mN increments. Further investigations were conducted at maximum indentation force F_{HL} varied between 1000 mN $\leq F_{HL} \leq$ 1750 mN with $\Delta F_{HL} = 250$ mN increments. For each coated variant and the corresponding maximum indentation force F_{HL}, four measurements were conducted. A conical diamond indenter with an effective opening angle of $\Theta = (60 \pm 5)°$ and a nominal radius of $r = 10$ µm, mounted on the high-load sensor of the UNAT nanoindenter from ASMEC GmbH, Dresden, Germany, was used for this purpose. During the quasi-static measurement, the indentation force was increased at a constant strain rate $\varepsilon = 0.05\ s^{-1}$. The indents were analyzed using SEM at GFE for surface cracks and delamination. Furthermore, the fracture toughness K_C was determined from the indentation imprints utilizing the Laugier model, according to the following Eq. [16]:

$$K_C = k^p \cdot (a/l)^{1/2} \cdot (E_{IT}/H_{IT})^{2/3} \cdot F_{HL} \Big/ c^{3/2}.$$

In this context, a represents the distance from the outline to the center of the indentation, l denotes the average crack length, and c is defined as the sum of a and l. The calibration constant k^P was chosen as $k^P = 0{,}015$ according to Laugier [16].

3. Results and discussion

3.1. Coating properties and compound adhesion

The chemical composition of the nanocomposite CrAlSiN coatings measured by EPMA is presented in Fig. 2. As the total silicon content c_{Si} increases from $c_{Si} = 5$ at.-% to $c_{Si} = 16$ at.-%, the nitrogen content c_N also rises slightly from $c_N = 47$ at.-% to $c_N = 52$ at.-%. Given that the Al/Cr ratio remains constant at approximately Al/Cr = 55/45, the metallic/nitrogen ratio (CrAlSi)/N adjusts in response to the increase in nitrogen. X-ray photoelectron spectroscopy (XPS) measurements conducted by Park et al. suggest that an increase in silicon content x_{Si} in CrAlSiN coatings results in a higher proportion of Si_3N_4 alongside the CrAlN lattice [17]. The increasing nitrogen content c_N in the present coatings could be attributed to this effect.

As measured by EPMA, the Si contents x_{Si} in the metal portion of the present CrAlSiN toplayers vary as follows: x_{Si} = 10, 16, 22, 29 at.-%, Table 2. Thereby, no significant standard deviation could be measured. According to that, the coating nomenclature was chosen as $(CrAlSi_{10})N$, $(CrAlSi_{16})N$, $(CrAlSi_{22})N$ and $(CrAlSi_{29})N$. (See Table 2.)

SEM images of the fracture cross-sections of the CrAlSiN coatings are presented in Fig. 3. The coating thickness is similar for all coatings,

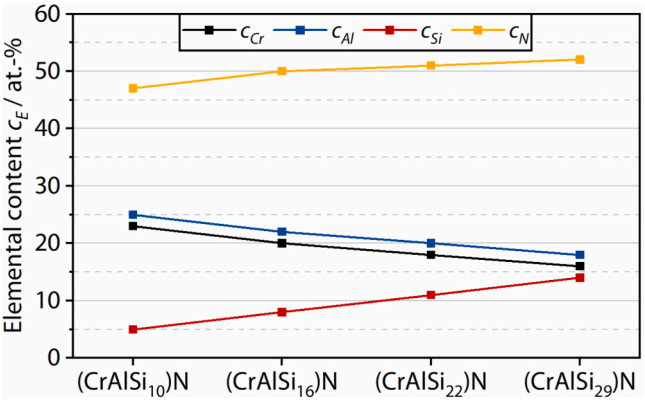

Fig. 2. Chemical composition of the CrAlSiN coatings acquired by EPMA.

Table 2
Chemical composition of the metal portion of CrAlSiN coatings acquired by EPMA.

Process	ID5189	ID5190	ID5191	ID5192
Nomenclature	$(CrAlSi_{10})N$	$(CrAlSi_{16})N$	$(CrAlSi_{22})N$	$(CrAlSi_{29})N$
Cr content x_{Cr} / at.-%	43	40	37	34
Al content x_{Al} / at.-%	47	44	41	37
Si content x_{Si} / at.-%	10	16	22	29

ranging from $S = 2.7$ µm to $S = 3.0$ µm. The morphology features a fine columnar CrAl/CrAlN interlayer and a dense CrAlSiN functional layer. The dense structure of the coatings may be attributed to an amorphous Si_3N_4 matrix present in the nanocomposite coatings. In addition to the morphology, the topography of the coatings is shown in Fig. 3. All coatings display a cauliflower-like topography, characterized by large clusters of the fine vertical columns within the interlayer, which are prominently featured by the dense functional layer above.

In addition to the SEM images of the coatings' topography, the area average roughness *Sa* and root mean square height *Sq* of the CrAlSiN coatings are presented in Table 3. The values reflect the similarity of the topography observed in Fig. 3. In conclusion, the high Si content x_{Si} does not appear to affect the coating morphology and topography.

To gain a deeper understanding of the microstructural evolution of the CrAlSiN coatings, transmission electron microscopy (TEM) investigations were conducted. Fig. 4 presents cross-sectional TEM bright-field (BF) micrographs along with corresponding selected area electron diffraction (SAED) patterns. The SAED patterns indicate that the crystallites are oriented along the (111), (200), and (220) directions, with a preferential orientation in the (111) and (200) directions. All coatings exhibit a crystalline interlayer. The $(CrAlSi_{10})N$ and $(CrAlSi_{16})N$ coatings display a fine-grained structure with a columnar arrangement, which transitions to an amorphous structure at a silicon content of $x_{Si} =$ 22 at.-%. A nanolaminar structure is evident in all coatings, resulting from table rotation in front of the individual cathodes. The SAED pattern for the $(CrAlSi_{10})N$ coating consists of elongated arc-shaped spots distributed around the circumference of the diffraction rings, indicative of relatively large crystallites with limited orientations. As the silicon content increases, these arcs elongate and form continuous diffraction rings, suggesting significantly smaller crystalline domains with random orientation distributions. This effect is particularly pronounced in the SAED patterns of the $(CrAlSi_{22})N$ and $(CrAlSi_{29})N$ coatings, which show diffuse diffraction rings corresponding to (111), (200), and (220) planes against an amorphous halo background. These observed changes in the SAED patterns confirm that a two-phase amorphous-nanocrystalline structure develops within the CrAlSiN coatings, with an increasing volume fraction of the amorphous Si_3N_4 phase as silicon content rises.

Fig. 5 shows the Rockwell indentations on the CrAlSiN/WC-Co composites. It is evident that the excellent interfacial adhesion of the coating remains intact even with increasing silicon content. Therefore, the silicon content does not have a significant impact on the interfacial adhesion under static loading.

The CLSM images of the scratches created during the scratch test, as shown in Fig. 6, exhibit similar results. The critical load *Lc1* is consistent across all coatings at *Lc1* = 40 N. Since this value is not particularly significant for the present investigation, a higher resolution of the constant load measurements at this point was omitted. Even at the highest load permissible according to the standard $F_N = 100$ N, there is no evidence of spalling at the scratch edge or penetration into the substrate at the scratch base. Therefore, the coating adhesion can also be assessed as excellent in this case and is independent of the silicon content.

3.2. Elastic-plastic properties

Fig. 7 presents the indentation hardness H_{IT} and indentation modulus E_{IT} measured via nanoindentation for the CrAlSiN coatings. For the $(CrAlSi_{10})N$ coating, the indentation hardness is measured as $H_{IT} = (26.3 \pm 2.0)$ GPa, while the indentation modulus is $E_{IT} = (267.0 \pm 5.3)$ GPa, see Table 4. Kolesnikov et al. recorded comparable values for a CrAlSiN coating with $x_{Si} = 7$ at.-%, reporting $H_{IT} = 24.1$ GPa and $E_{IT} = 251.3$ GPa [18]. The presence of an amorphous Si_3N_4 phase may inhibit grain growth, initially resulting in a fine-grained structure. Therefore, the grain size is below the critical value d < 10 nm for the Hall-Petch relationship [19]. The high hardness of the nanocomposites is consequently attributed to the amorphous matrix [20]. CrAlSiN coatings deposited by Tritremmel et al. via arc PVD, exhibit an increase in hardness up to a silicon content $x_S = 10$ at.-%, followed by a significant decrease at $x_{Si} = 20$ at.-% [21]. However, this effect is not evident in the current investigations. The indentation hardness H_{IT} values in this study are similar across all four coatings, ranging within $H_{IT} = (25.5 \pm 1.6)$ GPa. This finding suggests that while silicon may contribute to certain

Table 3
Area average roughness *Sa* and root mean square height *Sq* of the CrAlSiN coatings acquired by CLSM.

Roughness	$(CrAlSi_{10})N$	$(CrAlSi_{16})N$	$(CrAlSi_{22})N$	$(CrAlSi_{29})N$
Area average roughness *Sa* / µm	0.03	0.03	0.02	0.02
Root mean square height *Sq* / µm	0.05	0.05	0.03	0.03

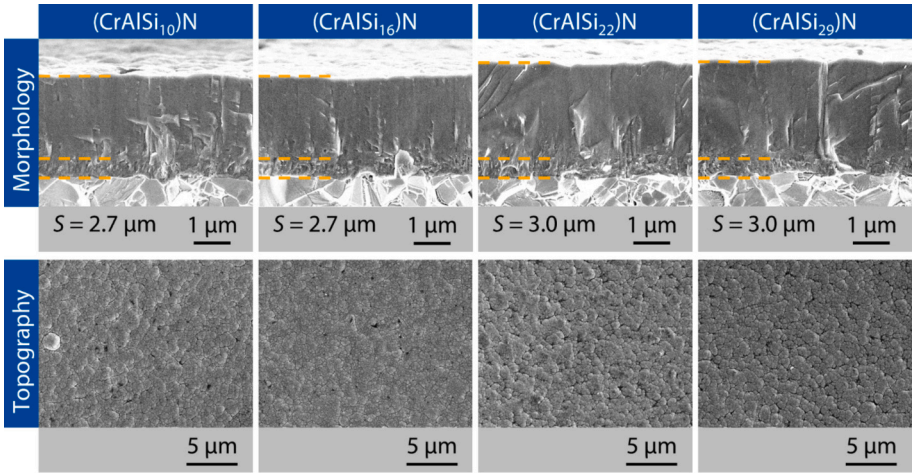

Fig. 3. SEM images of morphology and topography of the CrAlSiN coatings.

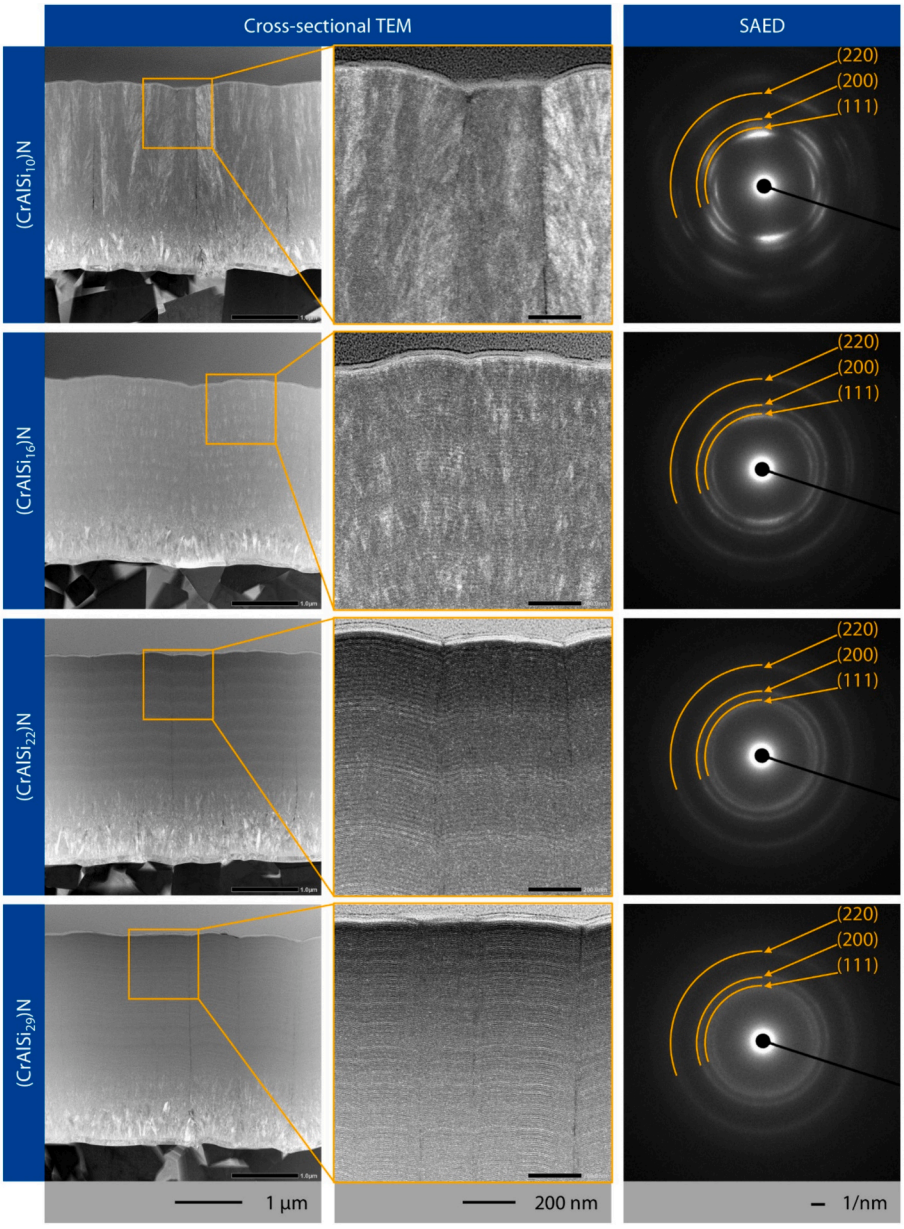

Fig. 4. Cross-sectional TEM BF micrographs and SAED patterns of the CrAlSiN coatings.

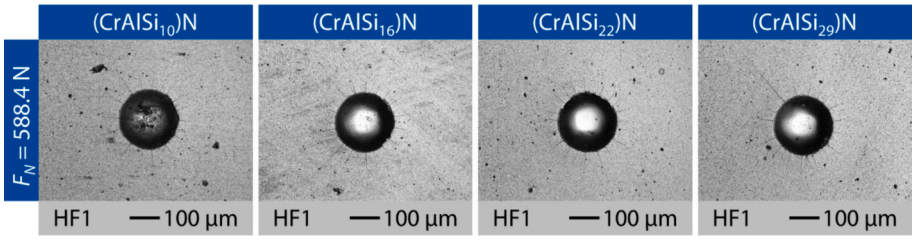

Fig. 5. CLSM images of Rockwell indent imprints at F_N = 588.4 N and adhesion strength class (HF) on the CrAlSiN coatings on WC-Co substrate.

structural characteristics within the coating, it does not significantly enhance its hardness. This could imply that other factors, such as the overall microstructure or phase composition, play a more critical role in determining hardness than silicon concentration alone. The absence of a decrease in H_{IT} values cannot be conclusively explained. However, it may be attributed to a higher proportion of dcMS power utilized during the coating process to achieve an increased silicon content. Previous studies examining the influence of silicon content on the hardness of CrAlSiN coatings have also been conducted on coatings deposited using arc PVD. Therefore, a further explanation could be that the application of HPPMS technology may result in the formation of a different coating structure due to its lower ionization energy. When further examining the results of the nanoindentation, only a slight increase in the indentation modulus E_{IT} is observed with increasing Si content, with E_{IT} = (267.0 ±

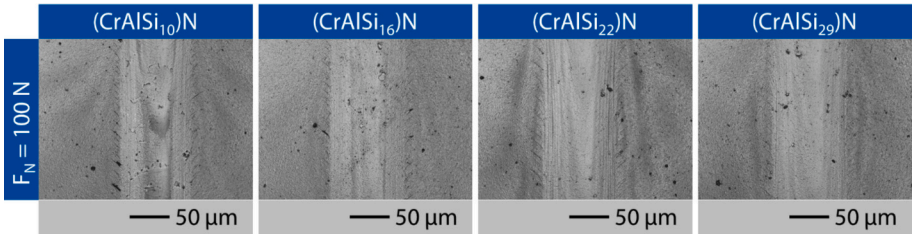

Fig. 6. CLSM images of scratches at $F_N = 100$ N on the CrAlSiN coatings on WC-Co substrate.

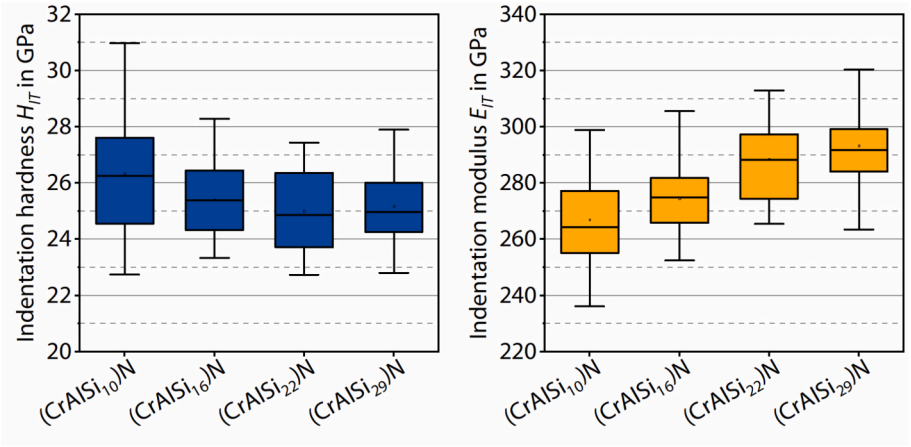

Fig. 7. Indentation hardness H_{IT} and modulus E_{IT} acquired by nanoindentation at maximum indentation force $F_{max} = 10$ mN.

Table 4
Elastic-plastic properties of the CrAlSiN coatings acquired by nanoindentation at maximum indentation force $F_{max} = 10$ mN.

Parameter	$(CrAlSi_{10})N$	$(CrAlSi_{16})N$	$(CrAlSi_{22})N$	$(CrAlSi_{29})N$
Indentation hardness H_{IT} / GPa	26.3 ± 2.0	25.4 ± 1.3	25.0 ± 1.2	25.2 ± 1.2
Indentation modulus E_{IT} / GPa	267.0 ± 15.3	274.4 ± 12.3	288.4 ± 12.9	293.3 ± 11.8
Max. depth d_{max} / nm	163.2 ± 5.3	163.5 ± 3,3	162.2 ± 3.8	161.4 ± 3.2
Residual depth d_0 / nm	65.6 ± 4.8	67.8 ± 3.1	72.6 ± 3.8	**3.8 ± 3.1**

15.3) GPa for the $(AlCrSi_{10})N$ coating, rising to $E_{IT} = (293.3 \pm 11.9)$ GPa for the $(AlCrSi_{29})N$ coating, see Table 4. An increase in the indentation modulus E_{IT} may be associated with a dense microstructure. This structure is promoted by the formation of phases such as nanocrystalline CrAlN or amorphous Si_3N_4 in nanocomposite CrAlSiN observes in TEM analyses, Fig. 4. A higher indentation modulus indicates increased stiffness of the coatings, suggesting that the material is more resistant to elastic deformation. However, this enhanced stiffness may also be associated with greater brittleness, which could potentially compromise crack resistance.

The observation of the averaged indentation force-depth curves from the nanoindentation of the CrAlSiN coatings presented in Fig. 8 indicates that the curves do not exhibit significant differences. The only variations observed are in the unloading, which results in an increase of the residual depth d_0 from $d_0 = 65.6 \pm 4.8$ nm for the $(AlCrSi_{10})N$ coating to $d_0 = 73.8 \pm 3.1$ nm for the $(AlCrSi_{29})N$ coating, see Table 4. The increase in indentation modulus E_{IT} with higher Si content reflects enhanced elastic stiffness, while the unchanged indentation hardness H_{IT} indicates that the material's resistance to permanent deformation remains constant. At the same time, the greater residual indentation depth suggests facilitated plasticity. With increasing Si content, the coatings transform

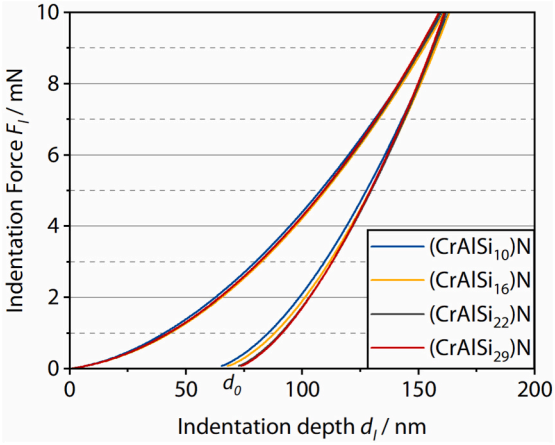

Fig. 8. Averaged indentation force - indentation depth curves of the CrAlSiN coatings acquired by nanoindentation at maximum indentation force $F_{max} = 10$ mN.

from fine-crystalline to amorphous structures. The increase in indentation modulus observed in the more amorphous coatings may be attributed to the fact that amorphous structures often exhibit denser atomic packing. At the same time, the amorphous structure may promote different plastic deformation mechanisms compared to crystalline materials, most notably, the absence of conventional dislocation activity and instead the formation of local shear bands. These shear bands can be activated more easily under load, which may lead to a greater residual indentation depth after unloading.

Plastic work percentage W_{pl} and elastic work percentage W_{el}, derived from the averaged indentation force-depth curves of the CrAlSiN coatings are shown in Fig. 9. There is only a slight increase in the proportion of plastic work W_{pl} with increasing silicon content in the CrAlSiN

coating. An increase in plastic work percentage with higher Si content reflects an enhanced capacity for plastic deformation. If a larger proportion of the total energy is dissipated through plastic deformation (i.e., a higher plastic work percentage), less energy remains available for elastic processes. Consequently, this correlates with the greater residual depth d_0 after unloading.

In summary, it must be stated that for all the elastic-plastic properties discussed before and presented in Table 4, the differences lie within the range of standard deviation or only slightly outside this range. Therefore, no significant differences can be identified between the coatings that would provide insights into the crack behavior of the coatings.

3.3. Cracking behavior under quasi-static normal loading

Table 5 presents the progression of crack occurrence across the high load indentation forces F_{HL} varied between 750 mN $\leq F_{HL} \leq$ 1000 mN with $\Delta F_{HL} = 50$ mN increments. It can be observed that cracking initiates at lower forces with increasing silicon content x_{Si}. For the ($CrAlSi_{10}$)N coating crack initiation starts at $F_{HL} = 1000$ mN whereas the onset for the ($CrAlSi_{29}$)N coating is at $F_{HL} = 800$ mN. This trend underlines that while increased stiffness is beneficial for resisting plastic deformation, it may also predispose these coatings to earlier crack initiation under specific stress conditions. The inherent brittleness associated with higher stiffness could lead to reduced resistance against crack propagation when subjected to significant loads. The small increments required to determine the start of cracking reflect the slight increase in the proportion of plastic work, see Fig. 9.

SEM images of the indent imprints and surface cracks at loads where first cracks were observed are shown in Fig. 10. The comparison of the images indicates that the initial crack formation is associated with a similar number cracks. The cracks spread radially from the edge of the indentation imprint. For the ($CrAlSi_{10}$)N coating, the cracks propagate along the column boundaries. These boundaries are also visible in the TEM images presented in Fig. 4, thereby providing a path of least resistance for crack propagation. For the other coatings, both the crack propagation through the columns and the crack lengths are similar.

With a further increase in the indentation force up to $F_{HL} = 1750$ mN, differences in crack formation among the coatings become apparent. The ($CrAlSi_{10}$)N coating with the lowest silicon content exhibits the most numerous and longest radial cracks still following the columns in most cases.

However, when the silicon content is increased to $x_{Si} = 16$ at.-%, these values initially decrease. With a subsequent increase in silicon content up to $x_{Si} = 29$ at.-%, the number of cracks, however, rises again.

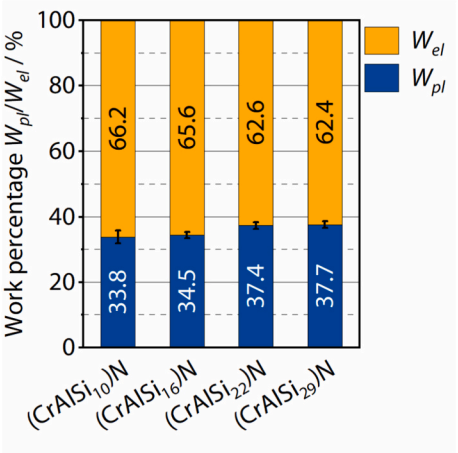

Fig. 9. Plastic work percentage W_{pl} and elastic work percentage W_{el} of the CrAlSiN coatings acquired by nanoindentation at maximum indentation force $F_{max} = 10$ mN.

Table 5
Crack occurrence in the CrAlSiN coatings acquired by nanoindentation with varying indentation force F_{HL}.

Indentation Force F_{HL} / mN	($CrAlSi_{10}$) N	($CrAlSi_{16}$) N	($CrAlSi_{22}$) N	($CrAlSi_{29}$) N
750	–	–	–	–
800	–	–	–	X
850	–	–	–	X
900	–	–	X	X
950	–	–	X	X
1000	X	X	X	X

- free from cracks X occurrence of cracks.

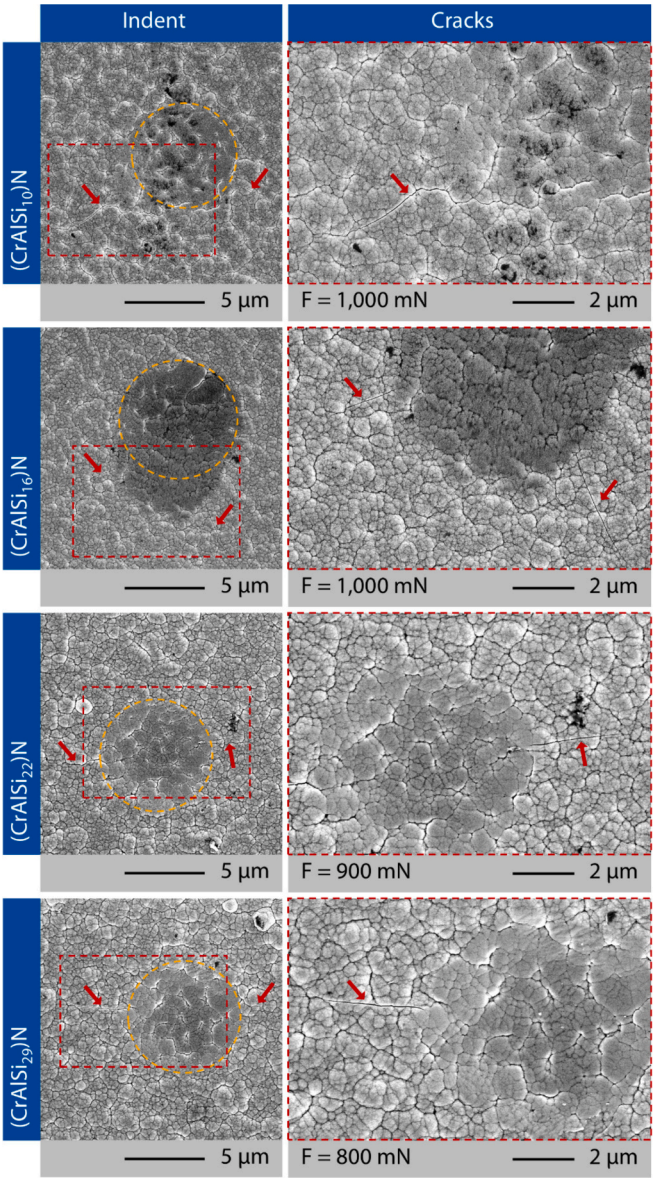

Fig. 10. SEM images of indent imprints and surface cracks for the CrAlSiN coatings acquired by high load nanoindentation at crack initiation.

The presented behavior was evident for all four indents of the respective high-load nanoindentation measurement. Further analysis of the fracture toughness K_C therefore was conducted using the SEM images presented in Fig. 11. The values for the distance from the outline to the center of the indentation a, the average crack length l, and c as the sum of a and l, along with the number of cracks n, are provided in Table 6.

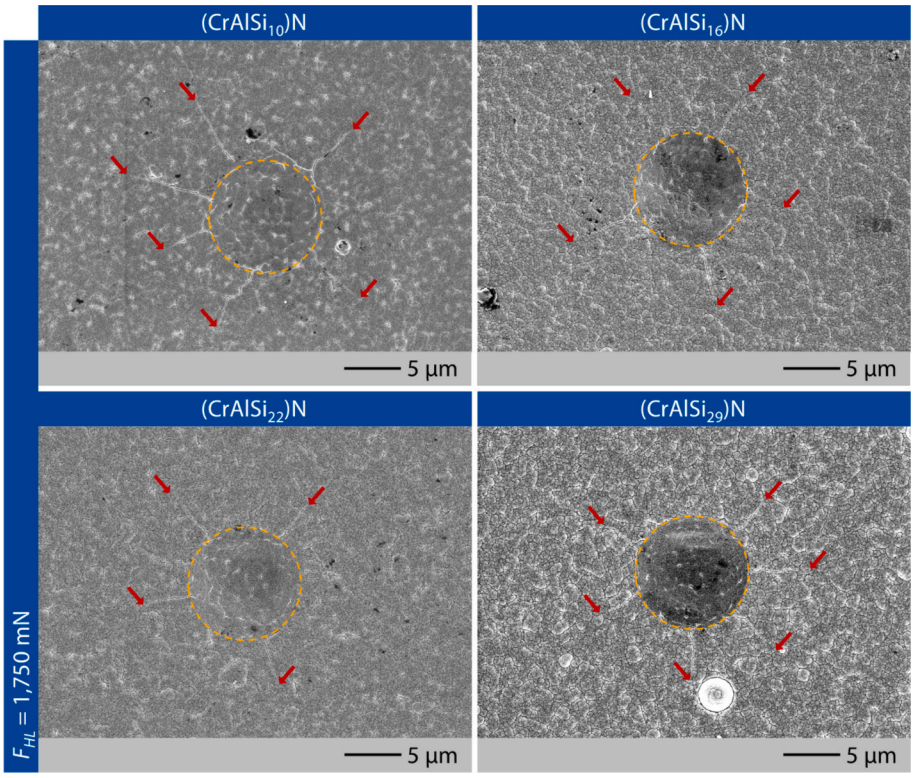

Fig. 11. SEM images of indent imprints and surface cracks for the CrAlSiN coatings acquired by high load nanoindentation at a maximum force $F_{HL} = 1750$ mN.

Additionally, the calculated fracture toughness K_C based on these values as well as the average indentation hardness H_{IT} and modulus E_{IT} from Table 4 is also presented in Table 6. As silicon content increases from $x_{Si} = 10$ at.-% to $x_{Si} = 22$ at.-%, there is a reduction in the number of cracks and an increase in K_C, suggesting that a higher proportion of amorphous phase enhance the structural integrity and toughness of the coatings. However, at $x_{Si} = 29$ at.-%, while K_C continues to rise slightly, the number of cracks returns to its previous level, indicating that excessive silicon may introduce brittleness or other adverse effects.

This counterintuitive result implies that there exists an optimal range of silicon concentration where crack growth is effectively mitigated due to enhanced interfacial adhesion or microstructural integrity provided by the Si_3N_4 matrix. However, beyond a certain threshold—linked to excessive brittleness—the material begins to fail more readily under stress.

4. Conclusion

In the investigations conducted, CrAlSiN coatings were deposited with varying silicon contents of $x_{Si} = 10$, 16, 22, 29 at.-% using HPPMS technology. The primary focus was on examining the mechanical properties and crack behavior of these nanocomposite coatings through normal load and high load nanoindentation.

The results indicate that there are no significant differences in hardness across all coatings. Similarly, the indentation modulus shows only a modest increase with higher silicon content, suggesting a slight enhancement in stiffness and a potentially more rigid microstructure due to higher proportions of the Si_3N_4 matrix. Additionally, while the proportion of plastic work increases slightly with higher silicon content, this indicates only a limited improvement. Notably, initial crack formation occurs at lower forces for coatings with elevated silicon levels and therefore more amorphous structure, highlighting a potential trade-off between stiffness and crack resistance. With a further increase in load to $F_{HL} = 1750$ mN, it is evident that the coating with a silicon content of $x_{Si} = 22$ at.-% displays the fewest and shortest cracks. This behavior implies an optimal range of silicon concentration where interfacial adhesion and microstructural integrity are effectively maintained.

Future work will focus on high-temperature nanoindentation studies conducted under both normal load conditions to determine indentation hardness H_{IT} and modulus E_{IT}, as well as under high load conditions to evaluate crack resistance at elevated temperatures 200 °C $\leq T \leq$ 600 °C. Additionally, milling tests with coated cutters are planned to further assess the performance of the coatings in practical machining applications. These investigations aim to provide a comprehensive understanding of the mechanical properties and durability of CrAlSiN coatings, ultimately contributing to their optimization for industrial use.

Table 6
Fracture toughness of CrAlSiN coatings at $F_{HL} = 1750$ mN.

Coating	a / µm	l / µm	c / µm	n / -	K_C / MPa · m$^{1/2}$
$(CrAlSi_{10})N$	4.9	5.5	10.4	6	2.5
$(CrAlSi_{16})N$	4.9	4.4	9.4	5	3.0
$(CrAlSi_{22})N$	4.9	4.5	9.3	4	3.2
$(CrAlSi_{29})N$	4.9	4.3	9.2	6	3.3

CRediT authorship contribution statement

Kirsten Bobzin: Writing – review & editing, Supervision, Resources, Project administration, Funding acquisition, Conceptualization. **Max Philip Möbius:** Writing – review & editing, Supervision, Project administration. **Jessica Borowy:** Writing – review & editing, Methodology, Investigation, Conceptualization.

Funding

The results presented were generated within the research project "Influence of high Si contents in nanocomposite coatings on the temperature-dependent elastic-plastic properties and the damage behaviour of milling tools" (BO 1979/96–1). This project was financially

supported by the German Research Foundation, Deutsche Forschungsgemeinschaft (DFG). The funding source had no involvement in study design, collection, analysis and interpretation of data as well as the writing and submission of the article.

Declaration of competing interest

The authors declare that they have no known competing financial interests or personal relationships that could have appeared to influence the work reported in this paper.

Acknowledgements

The authors gratefully acknowledge the financial support of the German Research Foundation, Deutsche Forschungsgemeinschaft (DFG), "Influence of high Si contents in nanocomposite coatings on the temperature-dependent elastic-plastic properties and the damage behaviour of milling tools", BO 1979/96-1, project number 516745377.

Code availability

Not applicable.

Data availability

The data that support the findings of this study are available from the corresponding author upon reasonable request.

References

[1] J.L. Endrino, S. Palacín, M.H. Aguirre, A. Gutiérrez, F. Schäfers, Determination of the local environment of silicon and the microstructure of quaternary CrAl(Si)N films, Acta Mater. 55 (2007) 2129–2135, https://doi.org/10.1016/j.actamat.2006.11.014.

[2] H.C. Barshilia, B. Deepthi, K.S. Rajam, Deposition and characterization of CrN/Si3N4 and CrAlN/Si3N4 nanocomposite coatings prepared using reactive DC unbalanced magnetron sputtering, Surf. Coat. Technol. 201 (2007) 9468–9475, https://doi.org/10.1016/j.surfcoat.2007.04.002.

[3] S. Vepřek, Conventional and new approaches towards the design of novel superhard materials, Surf. Coat. Technol. 97 (1997) 15–22, https://doi.org/10.1016/S0257-8972(97)00279-X.

[4] D. Chaliampalias, N. Pliatsikas, E. Pavlidou, K. Kolaklieva, R. Kakanakov, N. Vouroutzis, P. Patsalas, E.K. Polychroniadis, K. Chrissafis, G. Vourlias, Compositionally gradient PVD CrAlSiN films: structural examination and oxidation resistance, Surf. Eng. 33 (2017) 612–618, https://doi.org/10.1080/02670844.2016.1187789.

[5] D. Chaliampalias, G. Vourlias, E. Pavlidou, K. Chrissafis, Examination of the oxidation resistance of Cr–Mo–V tool steel by thermal analysis, J. Therm. Anal. Calorim. 108 (2012) 677–684, https://doi.org/10.1007/s10973-011-2073-9.

[6] D. Chaliampalias, L. Kolaklieva, R. Kakanakov, K. Saltidou, C. Prochaska, V. Chitanov, T. Cholakova, H. Bahchedjiev, S. Sotiropoulos, D. Sazou, E. Pavlidou, E.K. Polychroniadis, K. Chrissafis, G. Vourlias, Thermal and corrosion resistance of nanocomposite gradient TiAlSiN films, J. Therm. Anal. Calorim. 123 (2016) 169–179, https://doi.org/10.1007/s10973-015-4961-x.

[7] Y. Hou, B. Li, C. Shao, D. Li, X. Yang, S. Gao, Effect of high-temperature annealing in air and N2 atmosphere on the mechanical properties of Si3N4 fibers, Mater. Sci. Eng. A 724 (2018) 502–508, https://doi.org/10.1016/j.msea.2018.03.083.

[8] M. Kawate, A. Kimura Hashimoto, T. Suzuki, Oxidation resistance of Cr1−XAlXN and Ti1−XAlXN films, Surf. Coat. Technol. 165 (2003) 163–167, https://doi.org/10.1016/S0257-8972(02)00473-5.

[9] C. Tritremmel, R. Daniel, C. Mitterer, P.H. Mayrhofer, M. Lechthaler, P. Polcik, Oxidation behavior of arc evaporated Al-Cr-Si-N thin films, J. Vac. Sci. Technol. A 30 (2012) 61501, https://doi.org/10.1116/1.4748802.

[10] A. Drnovšek, M. Rebelo de Figueiredo, H. Vo, A. Xia, S.J. Vachhani, S. Kolozsvári, P. Hosemann, R. Franz, Correlating high temperature mechanical and tribological properties of CrAlN and CrAlSiN hard coatings, Surf. Coat. Technol. 372 (2019) 361–368, https://doi.org/10.1016/j.surfcoat.2019.05.044.

[11] J.A. García, A. Claver, M. Marques, E. Almandoz, J. Fernández de Ara, J.F. Palacio, I. Azkona, Improvement of the Tribocorrosion properties of cemented carbide (WC-tic-co) samples with PVD coating, Coatings 12 (2022) 1884, https://doi.org/10.3390/coatings12121884.

[12] C.-C. Chang, H.-W. Chen, J.-W. Lee, J.-G. Duh, Development of Si-modified CrAlSiN nanocomposite coating for anti-wear application in extreme environment, Surf. Coat. Technol. 284 (2015) 273–280, https://doi.org/10.1016/j.surfcoat.2015.06.090.

[13] Y.-Y. Chang, H.-M. Lai, Wear behavior and cutting performance of CrAlSiN and TiAlSiN hard coatings on cemented carbide cutting tools for Ti alloys, Surf. Coat. Technol. 259 (2014) 152–158, https://doi.org/10.1016/j.surfcoat.2014.02.015.

[14] W.C. Oliver, G.M. Pharr, An improved technique for determining hardness and elastic modulus using load and displacement sensing indentation experiments, J. Mater. Res. 7 (1992) 1564–1583, https://doi.org/10.1557/JMR.1992.1564.

[15] S.J. Bull, Nanoindentation of coatings, J. Phys. D. Appl. Phys. 38 (2005) R393–R413, https://doi.org/10.1088/0022-3727/38/24/R01.

[16] M.T. Laugier, New formula for indentation toughness in ceramics, J. Mater. Sci. Lett. 6 (1987) 355–356, https://doi.org/10.1007/BF01729352.

[17] I.-W. Park, D.S. Kang, J.J. Moore, S.C. Kwon, J.J. Rha, K.H. Kim, Microstructures, mechanical properties, and tribological behaviors of Cr–Al–N, Cr–Si–N, and Cr–Al–Si–N coatings by a hybrid coating system, Surf. Coat. Technol. 201 (2007) 5223–5227, https://doi.org/10.1016/j.surfcoat.2006.07.118.

[18] V.I. Kolesnikov, v.d. Vereskun, O.V. Kudryakov, D.S. Manturov, O.N. Popov, E. S. Novikov, Technologies for improving the wear resistance of heavily loaded tribosystems and their monitoring, J. Frict. Wear 41 (2020) 169–173, https://doi.org/10.3103/S1068366620020051.

[19] J.E. Carsley, J. Ning, W.W. Milligan, S.A. Hackney, E.C. Aifantis, A simple, mixtures-based model for the grain size dependence of strength in nanophase metals, Nanostruct. Mater. 5 (1995) 441–448, https://doi.org/10.1016/0965-9773(95)00257-F.

[20] S. Vepřek, New development in superhard coatings: the superhard nanocrystalline-amorphous composites, Thin Solid Films 317 (1998) 449–454, https://doi.org/10.1016/S0040-6090(97)00665-2.

[21] C. Tritremmel, R. Daniel, M. Lechthaler, P. Polcik, C. Mitterer, Influence of Al and Si content on structure and mechanical properties of arc evaporated Al–Cr–Si–N thin films, Thin Solid Films 534 (2013) 403–409, https://doi.org/10.1016/j.tsf.2013.03.017.